MRS Advances (2025) 10:2245–2253
https://doi.org/10.1557/s43580-025-01395-5

ORIGINAL PAPER

Polarization-dependent phonons and excitons on two-step growth vertical MoS_2/WS_2 heterostructures by CVD

M. K. Indika Senevirathna[1] · Elycia Wright[1] · Xudong Zheng[2] · Robin Rouseau[1] · Kedar Johnson[1,3] · Selena Coye[1] · P. K. D. D. P. Pitigala[1,4] · Darrell G. Schlom[2,5,6] · Michael D. Williams[1]

Received: 23 May 2025 / Accepted: 15 September 2025 / Published online: 30 September 2025

Abstract

MoS_2/WS_2 heterostructures make them significant due to their ability to integrate the advantageous properties of both materials, thereby facilitating the emergence of novel functionalities. Achieving uniform, large-area layers and thoroughly exploring their properties for potential applications is essential. This research investigated the phonon and exciton characteristics of MoS_2/WS_2 heterostructures deposited using chemical vapor deposition (CVD) and metal–organic chemical vapor deposition (MOCVD) on sapphire and SiO_2 substrates and their individual layers. We employed polarized Raman and photoluminescence (PL) spectroscopy to analyze these materials. The study identified notable PL emissions characterized by overtone-like features in two distinct energy regions within the $MoS_2/WS_2/SiO_2/Si$ heterostructures. These emissions, denoted as X^{A1} and X^{A2}, were detected at 2.134 eV and 2.155 eV, respectively. In the heterostructure (MoS_2/WS_2) on sapphire and SiO_2/Si, the MoS_2 originated PL-extinction ratios are 1.6306 and 0.9638, respectively, and the WS_2 originated PL-extinction ratios are 1.055 and 0.8519, respectively.

Introduction

The recent rapid advancement of digital technology over the last two decades has created a commensurate, ever-increasing need for electronic devices with high performance/high computing power. In an effort to meet these demands, scientists are researching new materials to enhance the performance of existing electronics, while also searching for new technologies and alternative energy sources to address global warming and the energy crisis.

Layered transition-metal dichalcogenides (TMDs) have attracted significant attention due to their distinctive properties. These compounds, composed of transition metals (group IV, V, VI, VII, IX, and X) combined with chalcogens (S, Se, and Te), exhibit over 40 different variations [1, 2]. Their electronic structure, which can vary from metallic to semiconducting, offers a wide range of applications in electronics, optoelectronics, spintronics, sensors, energy storage, and energy conversion, demonstrating the vast potential and versatility of TMDs [3–8]. The shift from an indirect to a direct band gap in TMDs as their thickness decreases from bulk to monolayer creates exciting opportunities for applications in nanoscale electronic and optoelectronic devices [9]. Recent advancements suggest that TMDs could be promising alternatives to silicon (Si) in front-end-of-line (FEOL) technologies due to significant improvements in their performance characteristics. For example, short channel transistors based on monolayer MoS_2 has shown a high on-state current of 1.23 mA/μm under source-to-drain bias of 1 V, an on/off ratio over 10^8 and an intrinsic delay of 74 fs, outperforming equivalent silicon complementary metal–oxide–semiconductor technologies and satisfied the 2028 roadmap target [10]. Furthermore, the tunable bandgap and broad optical absorption properties of TMDs facilitate a variety of optoelectronic artificial synaptic devices, such as optogenetic neuromorphic

✉ M. K. Indika Senevirathna
imatara@cau.edu

1 Department of Physics, Clark Atlanta University, Atlanta, GA 30314, USA

2 Department of Materials Science and Engineering, Cornell University, Ithaca, NY 14853, USA

3 Department of Physics, Morehouse College, Atlanta, GA 30314, USA

4 Department of Physics, University of Sri Jayewardenepura, Nugegoda, Sri Lanka

5 Kavli Institute at Cornell for Nanoscale Science, Ithaca, NY 14853, USA

6 Leibniz-Institut für Kristallzüchtung, Max-Born-Str. 2, 12489 Berlin, Germany

devices and photo-tunable memory devices for neuromorphic computing [11].

Furthermore, the stacking of different layers of TMDs to form van der Waals heterostructures provides an excellent opportunity to enhance and tailor novel electronic and optoelectronic properties. For example, the type-II band alignment between two types of TMD monolayers-typically found in many TMD heterostructures—promotes the creation of interlayer excitons. This characteristic can be utilized to develop excitonic integrated circuits that could serve as the counterpart of electronic integrated circuits [12].

In our study, we studied the polarization-dependent phonons and excitons in MoS_2/WS_2 heterostructures grown on sapphire and SiO_2/Si substrates. The synthesis of molybdenum disulfide (MoS_2) and tungsten disulfide (WS_2) layers on silicon dioxide/silicon (SiO_2/Si) substrates was conducted utilizing the metal–organic chemical vapor deposition (MOCVD) technique with precisely controlled gas-phase precursors to improve uniformity in the PARADIM user facility at Cornell University [13, 14]. In addition, MoS_2, WS_2, and MoS_2/WS_2 layers were grown on sapphire substrates and MoS_2 layers on WS_2/SiO_2/Si substrates, using a proprietary chemical vapor deposition system (CVD) at Clark Atlanta University.

Materials and methods

The MoS_2/WS_2 heterostructures were grown using a two-step method on two different substrates: Sapphire and SiO_2/Si. The CVD method was employed for the growth of MoS_2, WS_2, and MoS_2/WS_2 heterostructures on the sapphire substrates. In contrast, the MOCVD method was used to grow MoS_2 and WS_2 on SiO_2/Si substrates, followed by CVD to produce the MoS_2/WS_2 heterostructure on the SiO_2/Si substrate.

Detailed description is available in the Supplementary file under the Materials and Methods section.

Results and discussions

The supplementary Fig. S1 shows the confocal optical microscope images for each layer: (a) MoS_2/sapphire, (b) WS_2/sapphire, (c) MoS_2/WS_2/sapphire, (d) MoS_2/SiO_2/Si, (e) WS_2/SiO_2/Si, and $MoS_2/WS_2/SiO_2$/Si. The confocal microscopy image of the monolayer films (samples labeled (a) and (b) above) implies full coverage on the substrate, and based on the uniformity of the image color and intensities, it is assumed to be a uniform film. Additionally, in the images of heterostructures, it was observed that MoS_2 is uniformly deposited on WS_2, forming a well-defined heterostructure on the sapphire substrate. For the heterostructure on the SiO_2/Si substrate, we found that MoS_2 uniformly covers a 1×2 cm^2 area of the WS_2 layer grown on the SiO_2/Si substrate using MOCVD.

Analysis of phonon modes by polarized raman spectra

Figure 1 shows unpolarized and both parallel and perpendicular polarized Raman spectra of the samples. In the case of parallel polarization, both the excitation and scattered electric field are in the *x* direction, while for cross-polarization, they are in the *x* and *y* directions. The supplementary Table S1 summarizes the phonon modes excited by the 532 nm laser for our samples MoS_2, WS_2, and MoS_2/WS_2 on sapphire and SiO_2/Si (shown in parentheses) substrates measured with the unpolarized light. As shown in Fig. 1a and Table S1, the Raman phonon modes were observed for MoS_2/sapphire at 179.0 cm^{-1}, 377.7 cm^{-1}, 384.2 cm^{-1}, 405.0 cm^{-1}, 417.0 cm^{-1}, 451.4 cm^{-1}, and 597.4 cm^{-1} and they were previously assigned to A_{1g} (M)-LA(M), $E'(M)^{LO_2}$, $E^1_{2g}(\Gamma)$, A_{1g} (Γ), A_{1g} (M), 2LA (M), and $E'(M)^{LO_2}$ + LA(M), respectively [15]. However, for our MoS_2 sample on a SiO_2/Si substrate (see Fig. 1d), in addition to the two dominant phonon modes observed at ~ 379 cm^{-1} [$E^1_{2g}(\Gamma)$], ~ 403.3 cm^{-1} [A_{1g} (Γ)], five additional Raman peaks were detected at 226 cm^{-1}, 272 cm^{-1}, 303 cm^{-1}, 360 cm^{-1}, and 432.5 cm^{-1}. Among these, the peak at 303 cm^{-1} is attributed to the transverse acoustic (TA) phonon mode originating from the underlying silicon substrate [16, 17]. The peak observed at 226 cm^{-1} [LA(M)] has been previously attributed to the partial oxidation of MoS_2 upon exposure to ambient conditions, leading to the formation of molybdenum oxides [18, 19]. Given that our MoS_2/SiO_2/Si sample has been measured after approximately three years, it is reasonable to expect the presence of molybdenum oxides due to this extended exposure to ambient environmental conditions and other aging-related degradation effects on the structure. Therefore, the observations regarding the MoS_2/SiO_2/Si are discussed separately as a case study in the supplementary document.

Similarly, the phonon modes observed for WS_2 on sapphire (see Fig. 1b) and on SiO_2/Si (see Fig. 1e) substrates, along with their assigned modes, are listed in Table S1. The number of layers in these four samples was determined by the peak frequency difference between $A_{1g}(\Gamma)$ (out-of-plane optical vibration of S atoms along the *c* axis) and $E^1_{2g}(\Gamma)$ (in-plane optical vibration of the Mo + S atoms in the basal plane) [16]. Our findings revealed the following differences and layer numbers: For MoS_2 on sapphire, the difference was 20.8 cm^{-1}, indicating a monolayer; for MoS_2 on SiO_2/Si, it was 24.3 cm^{-1}, corresponding to three layers; for WS_2 on sapphire, the difference was 65 cm^{-1}, signifying a monolayer; and for WS_2 on SiO_2/Si, it was 68.9 cm^{-1}, also indicative of three layers [20–22].

We then analyzed the Raman spectra of our vertical MoS_2/WS_2 heterostructures, which were grown on sapphire

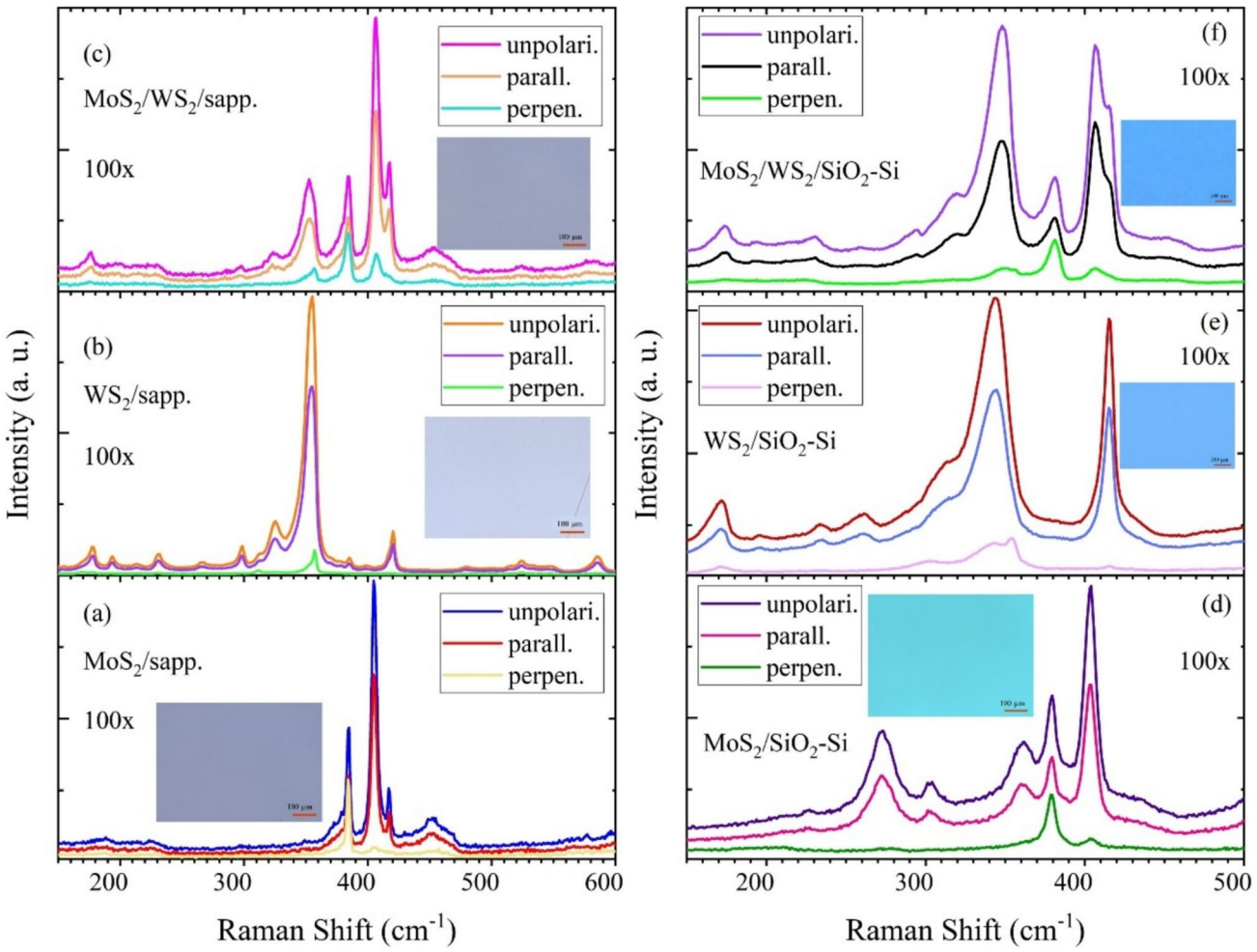

Fig. 1 Raman spectra of (a) MoS_2/sapphire, (b) WS_2/sapphire, (c) MoS_2/WS_2/sapphire, (d) MoS_2/SiO_2/Si, (e)WS_2/SiO_2/Si, and (f) $MoS_2/WS_2/SiO_2$/Si, collected under unpolarized, parallel-polarized (back scattering configuration z(x,x)z′ in the Porto notation), and perpendicular-polarized (back scattering configuration z(x,y)z′ in the Porto notation) light. The insert in each panel displays confocal optical microscope images of the corresponding layers, captured using a 20×objective lens. A 5 mW, 532 nm (2.33 eV) laser was used for excitation (under non-resonant)

(see Fig. 1c) and SiO_2/Si (see Fig. 1f) substrates using the CVD method. A summary of the phonon frequencies and their corresponding modes can be found in Table S1. The detected peaks at 175.4 cm^{-1} (173.0 cm^{-1}), 198.4 cm^{-1} (194.0 cm^{-1}), 296.5 cm^{-1} (293.9 cm^{-1}), 322.8 cm^{-1} (315.8 cm^{-1}), 348.9 cm^{-1} (343.3 cm^{-1}), 354.0 cm^{-1} (349.8 cm^{-1}), 417.0 cm^{-1} (415.8 cm^{-1}), and 588.4 cm^{-1} (578.3 cm^{-1}) can be ascribed to the $E'(M)^{TO_2} - LA(M)$, $E'(M)^{LO_2} - LA(M)$, $2LA(M) - 2E^2_{2g}(M)$, $E''(M)^{TO_1}$, 2LA(M), $E^1_{2g}(\Gamma)$, $A_{1g}(\Gamma)$ and $A_{1g}(M) + LA(M)$ phonon modes of the WS_2 film, respectively. Additionally, the peaks located at 224.5 cm^{-1} (230.5 cm^{-1}), 379.5 cm^{-1} (376.8 cm^{-1}), 384.3 cm^{-1} (381.7 cm^{-1}), 406.4 cm^{-1} (406.9 cm^{-1}), and 453.0 cm^{-1} (452.0 cm^{-1}) can be ascribed to the LA (M), $E'(M)^{LO_2}$, $E^1_{2g}(\Gamma)$, $A_{1g}(\Gamma)$ and 2LA(M) phonon modes of MoS_2 layers, respectively. These results confirm that the layers formed are heterostructures of MoS_2 and WS_2.

The full width at half maximum (FWHM) values for the $E^1_{2g}(\Gamma)$ and $A_{1g}(\Gamma)$ modes in TMDs layers are effective indicators of crystalline quality [23]. This study employed Renishaw wire software to analyze the Raman spectra of MoS_2, WS_2, and MoS_2/WS_2 layered materials deposited on both sapphire and SiO_2/Si substrates. This analysis enabled accurate determination of the FWHM values, phonon mode positions, and peak intensities. A comprehensive summary of the fitting results for both unpolarized and polarized light is presented in Tables S2 and S3, as well as Table 1. For the MoS_2 layers on sapphire, a low FWHM values were found at 2.8 cm^{-1} for the $E^1_{2g}(\Gamma)$ mode and 5.0 cm^{-1} for the $A_{1g}(\Gamma)$ mode, indicating high crystalline quality. In the case of WS_2

Table 1 Summary of phonon modes identified via Raman Spectra measured under unpolarized, parallel-polarized (back scattering configuration z(x,x)z′ in the Porto notation), and perpendicular-polarized (back scattering configuration z(x,y)z′ in the Porto notation), light for MoS_2/WS_2 heterostructures on sapphire and on SiO_2/Si substrates. Here, the values given in parentheses correspond to the MoS_2/WS_2 grown on the SiO_2/Si substrate

MoS_2/WS_2/sapphire ($MoS_2/WS_2/SiO_2$/Si)									
Phonon modes	Unpolarized			Parallel-polarized z(x,x)z′			Perpendicular polarizad z(x,y)z′		
Phonon mode [material of origin]	Posi. (cm^{-1})	FWHM (cm^{-1})	$A_{1g}(\Gamma)/E^1_{2g}(\Gamma)$ ratio	Posi. (cm^{-1})	FWHM (cm^{-1})	$A_{1g}(\Gamma)/E^1_{2g}(\Gamma)$ ratio	Posi. (cm^{-1})	FWHM (cm^{-1})	$A_{1g}(\Gamma)/E^1_{2g}(\Gamma)$ ratio
$E'(M)^{TO_2} - LA(M)$ [WS_2]	175.4 (173.0)	10.2 (15.0)	WS_2 originated: Height: 2.0 (1.04) Area: 2.02 (0.995)	175.5 (173.2)	6.6 (13.5)	WS_2 originated: Height:1.92 (1.24) Area: 2.03 (1.23)	–		WS_2 originated: Height: 0.597 (–) Area: 1.60 (–) MoS_2 originated: Height: 0.640 (0.425) Area: 1.20 (1.31)
$E'(M)^{LO_2} - LA(M)$	198.4 (194.0)	24.1 (10.9)		– (194.6)	– (12.1)		–		
	224.5 (230.5)	21.8 (10.5)		– (230.2)	– (10.5)		– (222.7)	– (20.2)	
$2LA(M) - 2E^2_{2g}(M)$	296.5 (290.4)	8.4 (12.4)	MoS_2 originated: Height:3.76 (4.91) Area: 7.69 (9.24)	294.7 (290.6)	24.9 (13.2)	MoS_2 originated: Height: 4.02 (4.87) Area: 7.97 (8.72)	–		
$E''(M)^{TO_1}$ [WS_2]	322.8 (317.3)	14.8 (26.4)		323.1 (318.2)	16.9 (27.8)		– (314.0)	– (42.6)	
2LA(M)[WS_2]	348.9 (343.7)	15.5 (18.5)		349.0 (344.2)	17.3 (18.3)		351.9 (–)	10.2 (–)	
$E^1_{2g}(\Gamma)$[WS_2]	354.0 (350.0)	7.7 (8.2)		353.9 (350.0)	7.7 (7.9)		356.7 (350.4)	**3.3** (22.6)	
$E'(M)^{LO_2}$ [MoS_2]	379.5 (376.3)	13.5 (14.5)		379.0 (375.6)	15.9 (15.6)		379.9 (375.3)	7.9 (14.2)	
$E^1_{2g}(\Gamma)$[MoS_2]	384.3 (381.6)	4.1 (6.2)		384.2 (381.3)	4.2 (6.5)		384.1 (381.2)	4.4 (7.1)	
$A_{1g}(\Gamma)$[MoS_2]	406.4 (406.9)	6.4 (10.1)		406.4 (406.7)	6.4 (9.7)		406.9 (407.2)	6.6 (14.9)	
$A_{1g}(\Gamma)$[WS_2]	417.0 (415.8)	5.3 (6.5)		417.0 (415.6)	5.5 (6.9)		415.9 (-)	**8.4** (–)	
2LA(M)	453.0 (453.1)	29.8 (17.4)		452.5 (452.4)	30.3 (19.2)		453.0 (447.2)	27.2 (30.8)	
$A_{1g}(M) + LA(M)$[WS_2]	588.4 (578.3)	76.5 (16.5)		587.2 (578.9)	29.9 (8.2)		–	–	

layers grown on sapphire, we observed the FWHM values of 6.9 cm^{-1} for the $E^1_{2g}(\Gamma)$ mode and 4.5 cm^{-1} for the $A_{1g}(\Gamma)$ mode, which again reflects a high crystalline quality. In contrast, the FWHM values for WS_2 on the SiO_2/Si substrate were notably higher, at 13.4 cm^{-1} for the $E^1_{2g}(\Gamma)$ mode and 7.3 cm^{-1} for the $A_{1g}(\Gamma)$ mode, further indicating that the sapphire substrate facilitates improved crystallinity for WS_2.

The analysis of the MoS_2/WS_2 heterostructure on sapphire yielded FWHM values of 4.1 cm^{-1} for the $E^1_{2g}(\Gamma)$ mode and 6.4 cm^{-1} for the $A_{1g}(\Gamma)$ mode in the MoS_2 layer. In the corresponding WS_2 layer, FWHM values of 7.7 cm^{-1} for the $E^1_{2g}(\Gamma)$ mode and 5.3 cm^{-1} for the $A_{1g}(\Gamma)$ mode were recorded. In contrast, the MoS_2/WS_2 heterostructure on the SiO_2/Si substrate exhibited FWHM values of 6.2 cm^{-1} for the $E^1_{2g}(\Gamma)$ mode and 10.1 cm^{-1} for the $A_{1g}(\Gamma)$ mode in the MoS_2 layer, while the WS_2 layer presented FWHM values of 8.2 cm^{-1} for the $E^1_{2g}(\Gamma)$ mode and 6.5 cm^{-1} for the $A_{1g}(\Gamma)$ mode. These findings further validate the superior crystalline quality of the MoS_2/WS_2 layers on sapphire. Overall, these findings highlight the importance of substrate choice in optimizing the crystallinity of TMD materials.

The textures of these films were analyzed using parallel and perpendicular polarized Raman spectra [24]. The peak ratio of $A_{1g}(\Gamma)/E^1_{2g}(\Gamma)$ was determined by fitting the Raman spectra for each parallel and perpendicular polarization, and those values are listed in Tables S2 and S3, and Table 1. Our study reveals that the intensity and area ratios of the $A_{1g}(\Gamma)/E^1_{2g}(\Gamma)$ Raman modes in MoS_2 films decrease under both parallel and cross-polarization configurations when changing the substrate from sapphire to SiO_2/Si. This behavior suggests a potential reorientation of the crystal grains from an out-of-plane to an in-plane alignment. In contrast, WS_2 films exhibit an increase in the $A_{1g}(\Gamma)/E^1_{2g}(\Gamma)$ ratio under parallel polarization upon the same substrate transition, indicating a tendency toward out-of-plane grain orientation. Notably, the $A_{1g}(\Gamma)$ mode is not observed under cross-polarization for WS_2 on SiO_2/Si. In MoS_2/WS_2 heterostructures, the ratio of $A_{1g}(\Gamma)/E^1_{2g}(\Gamma)$ for MoS_2 increases with the substrate change for both polarization configurations, whereas WS_2 exhibits a decrease under parallel polarization, suggesting a contrasting reorientation behavior within the heterostructure.

Analysis of polarized-PL spectra

Figures 2 and 3 present the measured and fitted PL spectra for our films on sapphire and SiO_2/Si substrates under unpolarized, parallel polarized, and perpendicular polarized light. Table S3 summarizes the assigned PL peaks, and their energies observed for these films. The PL spectra of MoS_2 sapphire substrates are found to be exhibit three characteristic peaks—designated as A^-, A, and B—corresponding to the trion, the direct bandgap exfig

citon, and the excitonic transition associated with valence band splitting due to spin–orbit coupling in MoS_2, respectively [25– 27] A strong PL signal was observed for WS_2 on sapphire, with an intensity more than 20 times greater than that on SiO_2/Si and over 57 times stronger than the PL signal of MoS_2 on sapphire. Further, for the WS_2 on sapphire, only the A^- and A excitonic peaks were observed. In contrast, the WS_2/SiO_2/Si sample displayed an additional emission peak at 1.752 eV. This peak is attributed to either a biexciton (A^{xx}) or defect-related emissions, such as defect-bound excitons or other radiative processes associated with defects [27–29]. The photoluminescence spectrum of the heterostructure on sapphire shows three distinct emission peaks. The first two peaks, the A^- trion at 1.763 eV and the A exciton peak at 1.874 eV, are associated with MoS_2. The third peak, the A exciton peak at 1.975 eV, is related to WS_2. These confirm the presence of electronic transitions from both MoS_2 and WS_2 within the heterostructure. We observed notable PL emissions exhibiting repeated or overtone-like characteristics in two distinct energy regions within $MoS_2/WS_2/SiO_2$/Si heterostructures (see Fig. 3). In the first energy region, we identified the following PL peaks: The trion at 1.910 eV (WS_2), the A exciton at 1.941 eV (WS_2), and the A exciton at 1.867 eV (MoS_2). In the second region, the peaks at 2.134 eV and 2.155 eV are attributed to X^{A1} and X^{A2}, respectively. The origins of these two transitions remain under investigation. These emissions are assumed to be due to the B exciton in MoS_2, as it can arise from spin–orbit-splitting of the valence band, at K-point, which in general appears around 2.1 eV. These energies can slightly vary with strain, dielectric environment, and doping. The SiO_2/Si substrate can induce the strain and the necessary dielectric environment. Furthermore, the two nearby PL features can be one due to natural B-excitation and the other due to B-trions or special inhomogeneity of the 2D lattice, causing variations in strain. The ~ 20 meV separation (2.134 vs 2.155 eV) is a reasonable value to assume for trion or strain effects.

Upon comparing the PL spectra for each polarization, we found a shift (3–4 meV) between peak positions between the unpolarized and polarized spectra across all films. The extinction ratios (parallel to perpendicular (s/p)) of peak intensities for the A-type PL peaks for MoS_2 on sapphire and SiO_2/Si substrates are 0.9268 and 0.6437, respectively. Those ratios for WS_2 on sapphire and SiO_2/Si, respectively, are 1.1888 and 1.0499. In the heterostructure (MoS_2/WS_2) on sapphire and SiO_2/Si, the MoS_2 originated PL-extinction ratios are 1.6306 and 0.9638, respectively, and the WS_2 originated PL-extinction ratios are 1.055, and 0.8519, respectively.

Tabulated are the peak position, the full width at half maximum (FWHM), and $A_{1g}(\Gamma)/E^1_{2g}(\Gamma)$ ratios of the peak

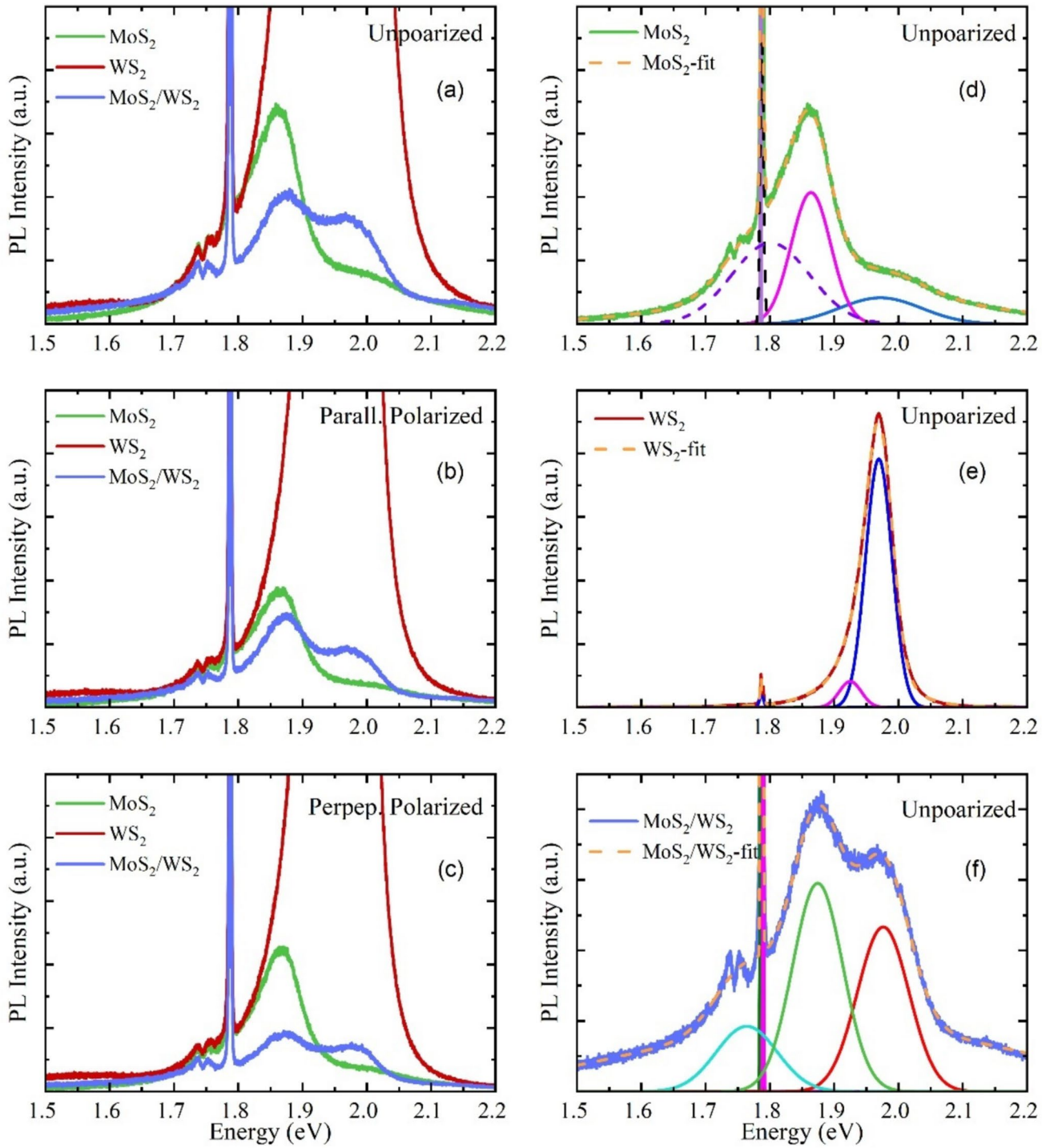

Fig. 2 Photoluminescence (PL) spectra of MoS_2, WS_2, and MoS_2/WS_2 on sapphire under (**a**) unpolarized, (**b**) parallel-polarized (back scattering configuration z(x,x)z′ in the Porto notation), and (**c**) perpendicular-polarized (back scattering configuration z(x,y)z′ in the Porto notation) light excitation. Panels (**d**)-(**f**) show the measured and deconvoluted PL spectra (unlabeled curves) under unpolarized excitation (curves shown in (**a**)) for (**d**) MoS_2, (**e**) WS_2, and (**f**) MoS_2/WS_2 on sapphire. A 0.5 mW, 532 nm (2.33 eV) laser served as the excitation source

intensity (height) and peak area for the two phonon modes relevant to each material (MoS_2 and WS_2) in MoS_2/WS_2 heterostructures on sapphire and on SiO_2/Si substrates, Here, the values presented in parentheses correspond to the 2D film(s) grown on the SiO_2/Si substrate.

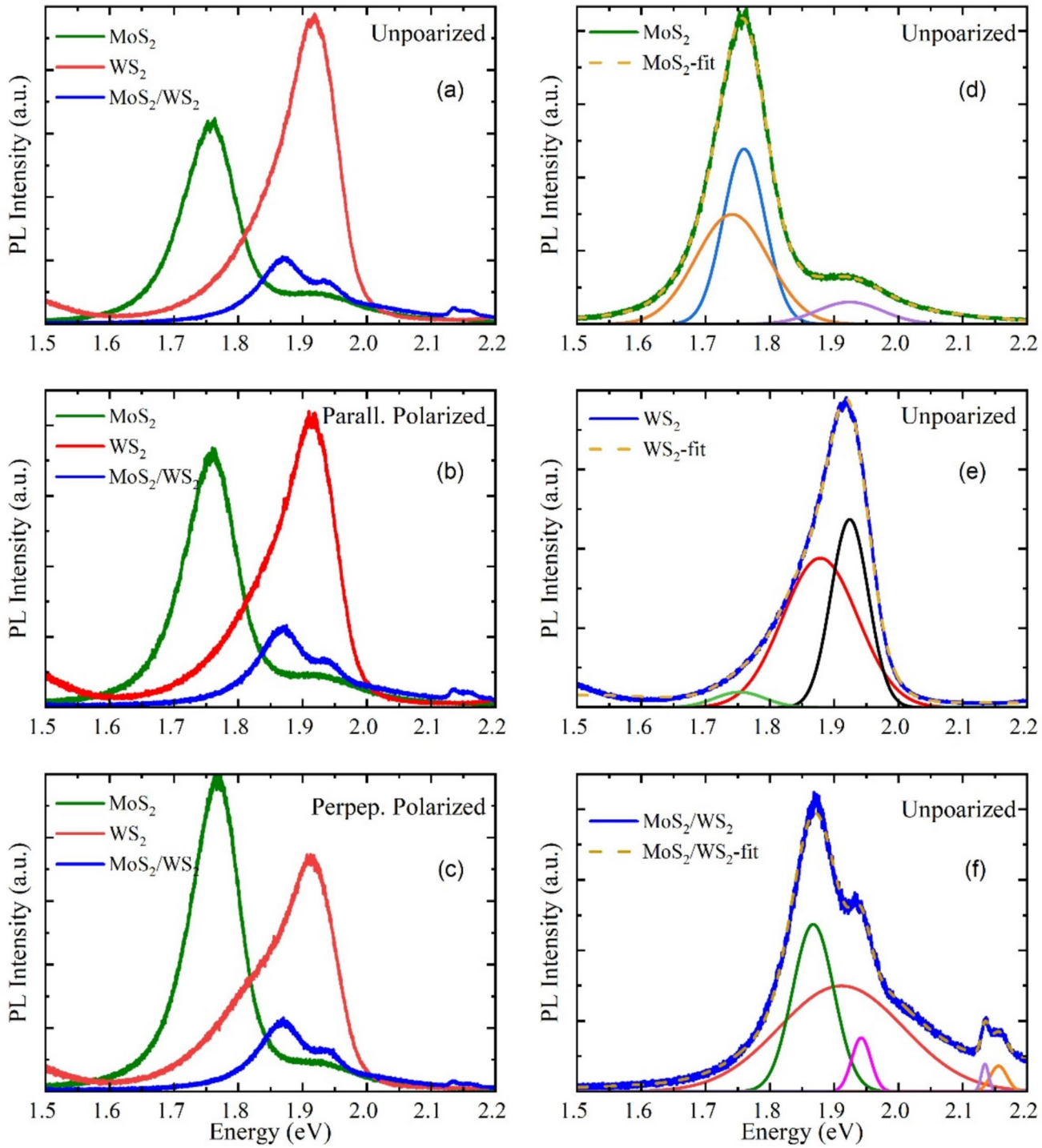

Fig. 3 Photoluminescence (PL) spectra of MoS_2, WS_2, and MoS_2/WS_2 on SiO_2/Si under (**a**) unpolarized, (**b**) parallel-polarized (back scattering configuration z(x,x)z′ in the Porto notation), and (**c**) perpendicular-polarized (back scattering configuration z(x,y)z′ in the Porto notation) light excitation. Panels (**d**)-(**f**) show the measured and deconvoluted PL spectra (unlabeled curves) under unpolarized excitation (the curves shown in (**a**)) for (**d**) MoS_2, (**e**) WS_2, and (**f**) MoS_2/WS_2 on SiO_2/Si. A 5 mW, 532 nm (2.33 eV) laser was used as the excitation source

Summary

This study explored the polarization-dependent phonons and excitons in MoS_2/WS_2 heterostructures synthesized on sapphire and SiO_2/Si substrates utilizing CVD and MOCVD. The confocal microscopy image of the film implies full coverage and a uniform film. Narrow Raman peaks imply good quality films with minimal defects.

Raman spectroscopy analysis indicated that the intensity and area ratios of the $A_{1g}(\Gamma)/E^1_{2g}(\Gamma)$ Raman modes in the MoS_2 films decreased under both parallel and cross-polarization configurations when transitioning the substrate from sapphire to SiO_2/Si. This phenomenon suggests a possible reorientation of the crystal grains from an out-of-plane alignment to an in-plane configuration. In contrast, the ratio for WS_2 displayed a trend toward out-of-plane orientation under parallel polarization conditions during the same substrate transition. The $WS_2/SiO_2/Si$ sample exhibited an additional emission peak at 1.752 eV, which may be attributed to biexcitons or defect-related emissions. The PL spectrum of the heterostructure on sapphire revealed three distinct emission peaks: The A^- at 1.763 eV and the A at 1.874 eV, associated with MoS_2, and the A peak at 1.975 eV, linked to WS_2. These results confirm the presence of electronic transitions involving both MoS_2 and WS_2 within the heterostructure. Furthermore, the study identified notable PL emissions characterized by overtone-like features in the $MoS_2/WS_2/SiO_2/Si$ heterostructures. These emissions, denoted as X^{A1} and X^{A2}, were detected at 2.134 eV and 2.155 eV, respectively. It is assumed to be due to the B exciton in MoS_2, from spin–orbit-splitting of the valence band at K-point, or due to the natural B-excitation and the B-trions.

The polarized-PL-extinction ratios (s/p) for the A-type PL in the MoS_2/WS_2 on sapphire and SiO_2/Si originated in MoS_2 and WS_2, respectively, are 1.6306, 0.9638, and 1.055, 0.8519.

Supplementary Information The online version contains supplementary material available at https://doi.org/10.1557/s43580-025-01395-5.

Acknowledgments The authors would like to express their gratitude to the Office of Naval Research HBCU/MI Faculty Start-up Program in Materials Physics- N00014-21-1-2823 and National Science Foundation -PREM-DMR-2122147. This work made use of the Thin Film Synthesis Facility of the Platform for the Accelerated Realization, Analysis, and Discovery of Interface Materials (PARADIM), which is supported by the National Science Foundation under Cooperative Agreement No. DMR-2039380. The authors acknowledge the use of VESTA software for crystal structure visualization in the graphical abstract. [K. Momma and F. Izumi, "VESTA 3 for three-dimensional visualization of crystal, volumetric and morphology data," J. Appl. Crystallogr., 44, 1272-1276 (2011)].

Author contributions M. K. Indika Senevirathna: Conceptualization (lead); Data curation (lead); Formal analysis (lead); Investigation (lead); Material growth by CVD (lead); Validation (lead); Visualization (lead); Writing—original draft (lead); Writing—review & editing (lead). Elycia Wright: Material growth by CVD (equal); Data curation (equal); Formal Analysis (equal); Validation (equal); Writing—review & editing (equal). Xudong Zheng: Material growth by MOCVD (lead); Investigation (equal); Validation (equal); Visualization (equal); Writing—review & editing (equal). Robin Rouseau: Material growth by CVD (equal); Visualization (equal); Writing—review & editing (equal). Kedar Johnson: Material growth by CVD (equal); Validation (equal); Visualization (equal); Writing—review & editing (equal). Selena Coye: Material characterization (supporting); Validation (equal); Writing—review & editing (equal). P. K. D. D. P. Pitigala: Validation (equal); Visualization (equal); Formal Analysis (equal); Writing—review & editing (equal); Darrell G. Schlom: Conceptualization (equal); Investigation (equal); Validation (equal); Visualization (equal); Writing—review & editing (equal); Funding acquisition (lead). Michael D. Williams: Conceptualization (equal); Investigation (equal); Validation (equal); Visualization (equal); Writing—review & editing (equal); Funding acquisition (lead).

Funding The Office of Naval Research HBCU/MI Faculty Start-up Program in Materials Physics- N00014-21-1-2823. National Science Foundation -PREM-DMR-2122147. National Science Foundation under Cooperative Agreement No. DMR-2039380.

Data availability The data that support the findings of this study are available from the corresponding author upon request.

Declarations

Conflict of interest The author has no conflicts to disclose.

References

1. X. Hu, L. Yan, L. Ding, N. Zheng, D. Li, T. Ji, N. Chen, J. Hu, Coord. Chem. Rev. **499**, 215504 (2024)
2. S. Joseph, J. Mohan, S. Lakshmy, S. Thomas, B. Chakraborty, S. Thomas, N. Kalarikkal, Mater. Chem. Phys. **297**, 127332 (2023). https://doi.org/10.1016/j.matchemphys.2023.127332
3. W. Choi, N. Choudhary, G.H. Han, J. Park, D. Akinwande, Y.H. Lee, Mater. Today **20**(3), 116–130 (2017). https://doi.org/10.1016/j.mattod.2016.10.002
4. R. Kappera, D. Voiry, S.E. Yalcin, B. Branch, G. Gupta, A.D. Mohite, M. Chhowalla, Nat. Mater. **13**(12), 1128–1134 (2014). https://doi.org/10.1038/nmat4080
5. Y.-R. An, X.-L. Fan, Z.-F. Luo, W.-M. Lau, Nano Lett. **17**(1), 368–376 (2017). https://doi.org/10.1021/acs.nanolett.6b04324
6. N. Huo, J. Kang, Z. Wei, S.-S. Li, J. Li, S.-H. Wei, Adv. Funct. Mater. **24**(44), 7025–7031 (2014). https://doi.org/10.1002/adfm.201401504
7. A. Sharma, R. Mahlouji, L. Wu, M.A. Verheijen, V. Vandalon, S. Balasubramanyam, J.P. Hofmann, W.M.M. Kessels, A.A. Bol, Nanotechnology **31**(25), 255603 (2020). https://doi.org/10.1088/1361-6528/ab7593
8. B. Kim, J. Kim, P.-C. Tsai, H. Choi, S. Yoon, S.-Y. Lin, D.-W. Kim, ACS Appl. Electron. Mater. **3**(6), 2601–2606 (2021). https://doi.org/10.1021/acsaelm.1c00192
9. R.A.B. Villaos, C.P. Crisostomo, Z.-Q. Huang, S.-M. Huang, A.A.B. Padama, M.A. Albao, H. Lin, F.-C. Chuang, NPJ 2D Mater. Appl. **3**(1), 2 (2019). https://doi.org/10.1038/s41699-018-0085-z

10. W. Li, X. Gong, Z. Yu, L. Ma, W. Sun, S. Gao, Ç. Köroğlu, W. Wang, L. Liu, T. Li, H. Ning, D. Fan, Y. Xu, X. Tu, T. Xu, L. Sun, W. Wang, J. Lu, Z. Ni, J. Li, X. Duan, P. Wang, Y. Nie, H. Qiu, Y. Shi, E. Pop, J. Wang, X. Wang, Nature **613**(7943), 274–279 (2023). https://doi.org/10.1038/s41586-022-05431-4
11. M. Naqi, Y. Cho, A. Bala, S. Kim, Mater. Today Electron. **5**, 100052 (2023). https://doi.org/10.1016/j.mtelec.2023.100052
12. Y. Jiang, S. Chen, W. Zheng, B. Zheng, A. Pan, Light Sci. Appl. **10**(1), 72 (2021). https://doi.org/10.1038/s41377-021-00500-1
13. K. Kang, S. Xie, L. Huang, Y. Han, P.Y. Huang, K.F. Mak, C.J. Kim, D. Muller, J. Park, Nature **520**(7549), 656–660 (2015). https://doi.org/10.1038/nature14417
14. X. Zheng, E. Gerber, J. Park, D. Werder, O. Kigner, E.-A. Kim, S. Xie, D.G. Schlom, Appl. Phys. Lett. (2021). https://doi.org/10.1063/5.0038383
15. X. Zhang, X.-F. Qiao, W. Shi, J.-B. Wu, D.-S. Jiang, P.-H. Tan, Chem. Soc. Rev. **44**(9), 2757–2785 (2015). https://doi.org/10.1039/C4CS00282B
16. K. Gołasa, M. Grzeszczyk, K. Korona, R. Bozek, J. Binder, J. Szczytko, A. Wysmolek, A. Babinski, Acta Physica Polonica Series A **124**, 849 (2013)
17. I. Parkhomenko, L. Vlasukova, F. Komarov, M. Makhavikou, O. Milchanin, A. Mudryi, E. Wendler, J. Phys. D Appl. Phys. (2022). https://doi.org/10.1088/1361-6463/ac526c
18. S. Mignuzzi, A. Pollard, N. Bonini, B. Brennan, I. Gilmore, M. Pimenta, D. Richards, D. Roy, Phys. Rev. B (2015). https://doi.org/10.1103/PhysRevB.91.195411
19. B.C. Windom, W.G. Sawyer, D.W. Hahn, Tribol. Lett. **42**(3), 301–310 (2011). https://doi.org/10.1007/s11249-011-9774-x
20. H. Zeng, G.-B. Liu, J. Dai, Y. Yan, B. Zhu, R. He, L. Xie, S. Xu, X. Chen, W. Yao, X. Cui, Sci. Rep. **3**(1), 1608 (2013). https://doi.org/10.1038/srep01608
21. C.-R. Wu, X.-R. Chang, C.-H. Wu, S.-Y. Lin, Sci. Rep. **7**(1), 42146 (2017). https://doi.org/10.1038/srep42146
22. A. Bera, A. K. Sood in MoS2: Materials, Physics, and Devices, edited by Z. M. Wang (Springer International Publishing, Cham, 2014), pp. 155–215.
23. S.E. Panasci, E. Schilirò, A. Koos, M. Nemeth, M. Cannas, S. Agnello, F. Roccaforte, B. Pécz, F. Giannazzo, Microelectron. Eng. **274**, 111967 (2023)
24. V. Vandalon, A. Sharma, A. Perrotta, B. Schrode, M.A. Verheijen, A.A. Bol, Nanoscale **11**(47), 22860–22870 (2019). https://doi.org/10.1039/C9NR08750H
25. K. Mak, K. He, C. Lee, G.-H. Lee, J. Hone, T. Heinz, J. Shan, Nature Mater. **12**, 207–211 (2013). https://doi.org/10.1038/nmat3505
26. S.S. Withanage, H. Kalita, H.-S. Chung, T. Roy, Y. Jung, S.I. Khondaker, ACS Omega **3**(12), 18943–18949 (2018). https://doi.org/10.1021/acsomega.8b02978
27. G. Plechinger, P. Nagler, J. Kraus, N. Paradiso, C. Strunk, C. Schüller, T. Korn, physica status solidi (RRL) – Rapid Res. Lett. **9**(8), 457–461 (2015)
28. M.A. Conway, J.B. Muir, S.K. Earl, M. Wurdack, R. Mishra, J.O. Tollerud, J.A. Davis, 2D Mater. **9**(2), 021001 (2022). https://doi.org/10.1088/2053-1583/ac4779
29. A. Soni, N.S. Kamath, Y.-Y. Shen, H. Seksaria, A. De Sarkar, W.-H. Chang, S.K. Pal, Sci. Rep. **15**(1), 7537 (2025). https://doi.org/10.1038/s41598-025-92188-1

Polarization-Dependent Phonons and Excitons on Two-Step Growth Vertical MoS_2/WS_2 Heterostructures by CVD

M. K. Indika Senevirathna[1, a)], Elycia Wright[1], Xudong Zheng[2], Robin Rouseau[1], Kedar Johnson[1,3], Selena Coye[1], P. K. D. D. P. Pitigala[1,4], Darrell G. Schlom[2,5,6], and Michael D. Williams[1]

[1]Department of Physics, Clark Atlanta University, Atlanta, Georgia, 30314, USA

[2]Department of Materials Science and Engineering, Cornell University, Ithaca, New York 14853, USA

[3]Department of Physics, Morehouse College, Atlanta, Georgia, 30314, USA

[4]Department of Physics, University of Sri Jayewardenepura, Nugegoda, Sri Lanka

[5]Kavli Institute at Cornell for Nanoscale Science, Ithaca, New York 14853, USA

[5]Leibniz-Institut für Kristallzüchtung, Max-Born-Str. 2, 12489 Berlin, Germany

[a)] Author to whom correspondence should be addressed: imatara@cau.edu

Materials and Methods:

The growth of MoS_2 or WS_2 on sapphire substrates was achieved through CVD using a quartz tube furnace with two separate heating zones. The growth of MoS_2 on sapphire was carried out by placing ~35 mg of MoO_3 powder in a boat located in the high-temperature zone of the furnace. A cleaned substrate was then positioned upside down above this boat, directly above the MoO_3 powder. Meanwhile, sulfur powder (~ 670 mg) was placed in a separate boat located in the low-temperature zone. The temperature for the MoO_3 source was set to 680 °C. An argon (Ar) mixture with 5% hydrogen (H_2) was used as the carrier gas, with a flow rate of 100 sccm. The same procedure and growth parameters were used to grow the second layer (MoS_2) on top of the first layer (WS_2) to form the heterostructure on sapphire and SiO_2/Si substrates.

In the case of WS_2 on sapphire growth, 30 mg of WO_3, mixed with 5 mg of KCl (seeding promoter), was placed in a boat, and the substrate was placed above it. The temperature of the mixture (WO_3 + KCl) was set at 1010 °C, and the carrier gas was Ar with a flow rate of 125 sccm. The temperature of the sulfur source was 250 °C. The growth process was consistently maintained for 30 minutes in all samples, while the growth chamber was maintained at atmospheric pressure.

The growth of MoS_2 and WS_2 on SiO_2/Si substrates by MOCVD was conducted in a 95 mm inner-diameter hot-wall quartz tube furnace. Molybdenum hexacarbonyl ($Mo(CO)_6$, MHC, Sigma-

Aldrich, 99.9%), tungsten hexacarbonyl ($W(CO)_6$, THC, Sigma-Aldrich, 99.9%), and diethyl sulfide ($(C_2H_5)_2S$, DES, Sigma-Aldrich, 98%) served as the precursors for Mo, W, and S, respectively, with argon as the carrier gas. For MoS_2 growth, the conditions were 600 °C, 5.98 Torr, with precursor flow rates of 6 sccm MHC, 0.3 sccm DES, 1 sccm H_2, and 1200 sccm Ar, over a duration of 2.25 hours. For WS_2, the growth was carried out at 635 °C and 6.38 Torr, using flow rates of 20 sccm THC, 1.6 sccm DES, 5 sccm H_2, and 1200 sccm Ar, for 3 hours. Sodium chloride was placed in the upstream region as a seeding promoter.

The samples were first observed, and their surface morphology was examined using a confocal laser optical microscope (Keyence-VK-X3000 3D profiler) with 100x objective lenses. Then, the samples were analyzed using a Raman microscope (Renishaw-inVia), which was capable of measuring the photoluminescence (PL) of the films in addition to Raman measurements. For the PL measurements, the laser was set to 0.5 mW at 532 nm with an objective at 100x, a 1.00 s exposure time, and 10 accumulations. For the Raman spectra, the laser was set to 5 mW at 532 nm with an objective at 100x, a 10.00 s exposure time, and 10 accumulations. The spot size is 0.763 μm.

An area of 2 × 2 cm^2 with good uniform coverage of MoS_2 spans on the sapphire substrate was selected for the second layer growth in the WS_2/MoS_2 heterostructure on sapphire, while an area of 1 × 2 cm^2 of WS_2 coverage was selected for MoS_2/WS_2 heterostructure on sapphire.

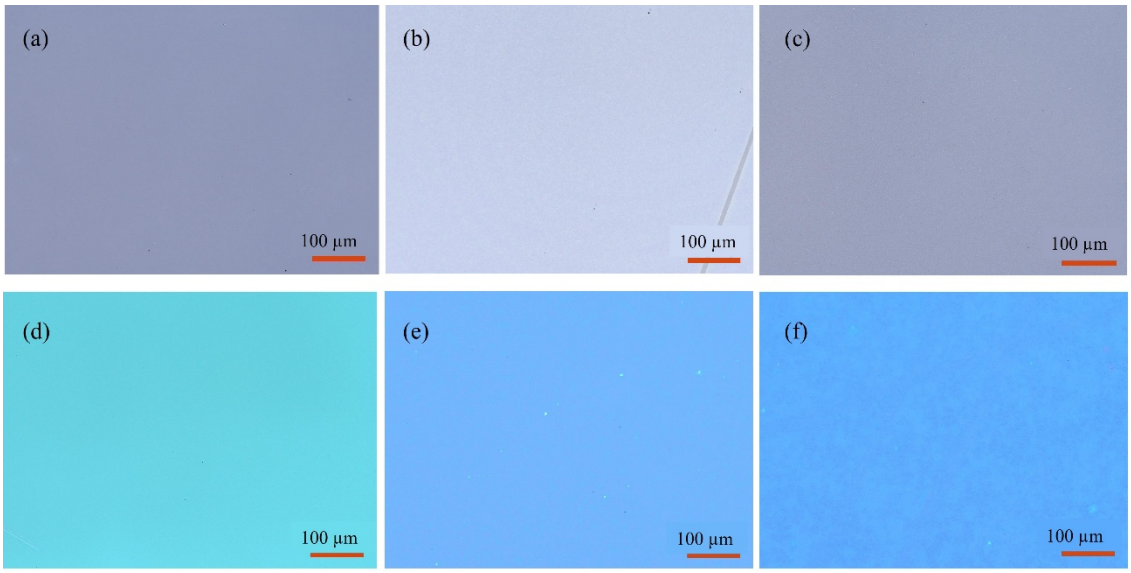

Fig. S1 Shows the confocal optical microscope image of the (a) MoS_2/sapphire, (b) WS_2/sapphire, (c) MoS_2/WS_2/sapphire, (d) MoS_2/SiO_2/Si, (e) WS_2/SiO_2/Si, and (f) $MoS_2/WS_2/SiO_2$/Si layers. The objective lens was 20x.

Table S1 Observed Raman phonon mode positions and corresponding mode assignments for MoS_2, WS_2, and MoS_2/WS_2 films on sapphire and SiO_2/Si substrates, measured using unpolarized light. Here, the frequencies indicated in parentheses correspond to the layers grown on the SiO_2/Si substrate.

	MoS_2/sapphire ($MoS_2/SiO_2/Si$)		WS_2/sapphire ($WS_2/SiO_2/Si$)		MoS_2/WS_2/sapphire ($MoS_2/WS_2/SiO_2/Si$)
Phonon mode	Peak (cm^{-1})	Phonon mode	Peak (cm^{-1})	Phonon mode	Peak (cm^{-1})
$A_{1g}(M) - LA(M)$	179.0	$E'(M)^{TO_2} - LA(M)$	176.9 (172.5)	$E'(M)^{TO_2} - LA(M)$ [WS_2]	175.4 (173.0)
LA(M)	(226)	$E'(M)^{LO_2} - LA(M)$	193.8 (196.1)	$E'(M)^{LO_2} - LA(M)$ [WS_2]	198.4 (194.0)
TO (M)	(272)	$E''(M)^{TO_1} - TA(M)$	213.3	LA (M) [MoS_2]	224.5 (230.5)
TA (Si)	(303)	$A_{1g}(M) - LA(M)$	231.1 (233.8)	$2LA(M) - 2E^2_{2g}(M)$ [WS_2]	296.5 (293.9)
TO(M)	(360)	$2LA(M) - 3E^2_{2g}(M)$	266.8 (259.0)	$E''(M)^{TO_1}$ [WS_2]	322.8 (315.8)
$E'(M)^{LO_2}$	377.7	$2LA(M) - 2E^2_{2g}(M)$	298.2	2LA(M) [WS_2]	348.9 (343.3)
$E^1_{2g}(\Gamma)$	384.2 (379)	*	312.4 (310.6)	$E^1_{2g}(\Gamma)$ [WS_2]	354.0 (349.8)
$A_{1g}(\Gamma)$	405.0 (403.3)	$E''(M)^{TO_1}$	325.2 (336.9)	$E'(M)^{LO_2}$ [MoS_2]	379.5 (376.8)
$A_{1g}(M)$	417.0	2LA(M)	349.5	$E^1_{2g}(\Gamma)$ [MoS_2]	384.3 (381.7)
*	(432.5)	$E^1_{2g}(\Gamma)$	354.9 (346.0)	$A_{1g}(\Gamma)$ [MoS_2]	406.4 (406.9)
2LA(M)	451.4	$A_{1g}(\Gamma)$	419.9 (414.9)	$A_{1g}(\Gamma)$ [WS_2]	417.0 (415.8)
$E'(M)^{LO_2} + LA(M)$	597.4	$A_{1g}(M) + LA(M)$	584.1 (575.8)	2LA(M) [MoS_2]	453.0 (452.0)
				$A_{1g}(M) + LA(M)$ [WS_2)]	588.4 (578.3)

*Not identified

Table S2 Summary of observed phonon mode positions, full width at half maximum (FWHM), and the intensity and area ratios of the $A_{1g}(\Gamma)/E^1_{2g}(\Gamma)$ for MoS_2 on sapphire and SiO_2/Si substrates, measured under unpolarized, parallel-polarized, and perpendicular-polarized light. Here, the frequencies indicated in parentheses correspond to the layers grown on the SiO_2/Si substrate.

MoS_2/sapphire ($MoS_2/SiO_2/Si$)									
Phonon modes	Unpolarized			Parallel polarized z(x, x)z′			Perpendicular polarizad z(x, y)z′		
	Posi. (cm^{-1})	FWHM (cm^{-1})	$A_{1g}(\Gamma)/E^1_{2g}(\Gamma)$	Posi. (cm^{-1})	FWHM (cm^{-1})	$A_{1g}(\Gamma)/E^1_{2g}(\Gamma)$ (cm^{-1})	Posi. (cm^{-1})	FWHM (cm^{-1})	$A_{1g}(\Gamma)/E^1_{2g}(\Gamma)$
$E'(M)^{LO_2}$	377.7	16.8	Height: 2.56 (2.73)	377.4	15.8	Height: 2.79 (2.81)	378.0	15.7	Height: 0.084 (0.125)
$E^1_{2g}(\Gamma)$	384.2 (379.0)	2.8 (6.1)		384.2 (379.0)	2.8 (5.7)		384.2 (379.0)	2.8 (6.3)	
$A_{1g}(\Gamma)$	405.0 (403.3)	5.0 (8.4)	Area: 5.77 (3.43)	405.0 (403.3)	5.0 (8.4)	Area: 6.80 (3.57)	405.2 (404.2)	6.6 (7.4)	Area: 0.519 (0.100)
$A_{1g}(M)$	417.0	3.4		417.0	2.9		452.4	20.7	
2LA(M)	451.4	30.0		451.4	26.6				
$E'(M)^{LO_2} + LA(M)$	597.4	28.3		597.7	11.9				

Table S3 Summary of observed phonon mode positions, full width at half maximum (FWHM), and the intensity and area ratios of the $A_{1g}(\Gamma)/E^1_{2g}(\Gamma)$ for WS_2 on sapphire and SiO_2/Si substrates, measured under unpolarized, parallel-polarized, and perpendicular-polarized light. Here, the frequencies indicated in parentheses correspond to the layers grown on the SiO_2/Si substrate.

WS_2/sapphire ($WS_2/SiO_2/Si$)									
Phonon modes	Unpolarized			Parallel polarized z (x, x) z′			Perpendicular polarizad z (x, y) z′		
	Posi. (cm^{-1})	FWHM (cm^{-1})	$A_{1g}(\Gamma)/E^1_{2g}(\Gamma)$	Posi. (cm^{-1})	FWHM (cm^{-1})	$A_{1g}(\Gamma)/E^1_{2g}(\Gamma)$	Posi. (cm^{-1})	FWHM (cm^{-1})	$A_{1g}(\Gamma)/E^1_{2g}(\Gamma)$
$E'(M)^{TO_2} - LA(M)$	176.9 (172.5)	7.5 (7.2)	Height: 0.174 (0.164)	176.9 (172.3)	7.2 (7.5)	Height: 0.176 (1.928)	172.1 (171.6)	14.7 (13.8)	Height: - (0.188)
$E'(M)^{LO_2} - LA(M)$	193.8 (196.1)	4.8 (5.6)		193.7 (195.7)	4.8 (6.5)		193.1 (191.4)	7.7 (4.4)	
$E''(M)^{TO_1} - TA(M)$	213.3	10.4	Area: 0.168 (1.295)	212.7	9.8	Area: 0.152 (1.474)	212.8	11.3	Area: - (0.517)
$A_{1g}(M) - LA(M)$	231.1 (233.8)	6.4 (11.9)		231.1 (234.0)	6.5 (14.7)		230.6	5.8	
$2LA(M) - 3E^2_{2g}(M)$	266.8 (259.0)	10.7 (15.8)		267.4 (258.6)	13.7 (16.0)		-	-	
$2LA(M) - 2E^2_{2g}(M)$	298.2	4.3		297.9	4.9		-	-	
	312.4 (310.6)	- (33.7)		- (313.1)	(39.2)		311 (303.2)	(30.8)	
$E''(M)^{TO_1}$	325.2 (336.9)	13.4 (22.9)		324.9 (338.9)	13.4 (21.3)		324.3	40.4	
$2LA(M)$	349.5	12.6		348.9	13.1		353.7 (343.0)	8.7 (27.4)	
$E^1_{2g}(\Gamma)$	354.9 (346.0)	6.9 (13.4)		354.6 (346.3)	7.1 (12.1)		357.1 (354.3)	2.6 (5.9)	
$A_{1g}(\Gamma)$	419.9 (414.9)	4.5 (7.3)		419.8 (414.9)	4.2 (7.3)		- (414.8)	- (11.4)	
$A_{1g}(M) + LA(M)$	584.1 (575.8)	9.3 (13.0)		585.0 (575.8)	9.2 (13.5)		584.3 (575.8)	8.4 (18.9)	

Table S4 Unpolarized photoluminescence peak energies, energy separations, and relative peak intensities obtained from spectral fitting of MoS_2, WS_2, and MoS_2/WS_2 on sapphire and SiO_2/Si substrates.

Peak label	**Peak Energy (eV)**		**Energy Separations (meV)**		**Peak Intensity (Counts)**	
MoS_2	**Sapphire**	**SiO_2/Si**	**Sapphire**	**SiO_2/Si**	**Sapphire**	**SiO_2/Si**
A^-	1.800	1.741	63	18	2557	4495
A	1.863	1.759	-	-	4147	7176
B	1.971	1.923	108	164	828	902
WS_2	**Sapphire**	**SiO_2/Si**	**Sapphire**	**SiO_2/Si**	**Sapphire**	**SiO_2/Si**
L or A^{xx}	-	1.752	-	125	-	975
A^-	1.924	1.877	-	-	24753	9423
A	1.969	1.923	45	46	235121	11863
MoS_2/WS_2	**Sapphire**	**SiO_2/Si**	**Sapphire**	**SiO_2/Si**	**Sapphire**	**SiO_2/Si**
A^-	1.763 (MoS_2)	1.910 (WS_2)	-	-	926	1500
A	1.874 (MoS_2)	1.867 (MoS_2)	-	-	2956	2373
A	1.975 (WS_2)	1.941 (WS_2)	-	-	2335	763
X^{A1}		2.134	-	-	-	390
X^{A2}		2.155	-	-	-	364

Table S5 Parallel polarized photoluminescence peak energies, energy separations, and relative peak intensities obtained from spectral fitting of MoS_2, WS_2, and MoS_2/WS_2 on sapphire and SiO_2/Si substrates.

Peak label	**Peak Energy (eV)**		**Energy Separations (meV)**		**Peak Intensity (Counts)**	
MoS_2	**Sapphire**	**SiO_2/Si**	**Sapphire**	**SiO_2/Si**	**Sapphire**	**SiO_2/Si**
A^-	1.796	1.743	69	18	1148	2530
A	1.865	1.761	-	-	2534	4152
B	1.973	1.926	108	165	387	447
WS_2	**Sapphire**	**SiO_2/Si**	**Sapphire**	**SiO_2/Si**	**Sapphire**	**SiO_2/Si**
L or A^{xx}	-	1.743	-	126	-	455
A^-	1.922	1.869	-	-	11930	4145
A	1.968	1.922	46	53	106776	5031
MoS_2/WS_2	**Sapphire**	**SiO_2/Si**	**Sapphire**	**SiO_2/Si**	**Sapphire**	**SiO_2/Si**
A^-	1.782 (MoS_2)	1.903 (WS_2)	-	-	667	768
A	1.874 (MoS_2)	1.865 (MoS_2)	-	-	2185	1306
A	1.974 (WS_2)	1.941 (WS_2)	-	-	1435	374
X^{A1}		2.134	-	-	-	202
X^{A2}		2.155	-	-	-	181

Table S6 Perpendicular polarized photoluminescence peak energies, energy separations, and relative peak intensities obtained from spectral fitting of MoS_2, WS_2, and MoS_2/WS_2 on sapphire and SiO_2/Si substrates.

Peak label	**Peak Energy (eV)**		**Energy Separations (meV)**		**Peak Intensity (Counts)**	
MoS_2	**Sapphire**	**SiO_2/Si**	**Sapphire**	**SiO_2/Si**	**Sapphire**	**SiO_2/Si**
A^-	1.823	1.746	45	22	1606	3015
A	1.868	1.768	-	-	2734	6450
B	1.999	1.922	131	154	331	480
WS_2	**Sapphire**	**SiO_2/Si**	**Sapphire**	**SiO_2/Si**	**Sapphire**	**SiO_2/Si**
L or A^{xx}	-	1.733	-	125	-	448
A^-	1.926	1.858	-	-	10035	3948
A	1.967	1.921	41	63	98642	4563
MoS_2/WS_2	**Sapphire**	**SiO_2/Si**	**Sapphire**	**SiO_2/Si**	**Sapphire**	**SiO_2/Si**
A^-	1.754 (MoS_2)	1.903 (WS_2)	-	-	458	703
A	1.873 (MoS_2)	1.865 (MoS_2)	-	-	1340	1355
A	1.978 (WS_2)	1.941 (WS_2)	-	-	1021	439
X^{A1}		2.134	-	-	-	125
X^{A2}		2.155	-	-	-	93

- **Case study: $MoS_2/SiO_2/Si$ aged film**

The Raman and PL spectra analysis of the aged MoS_2 film on SiO_2/Si substrate is separately presented here.

As of discussed earlier for our MoS_2 sample on a SiO_2/Si substrate (see Fig. 1(d)), in addition to the two dominant phonon modes observed at ~379 cm^{-1} [$E^1_{2g}(\Gamma)$], ~ 403.3 cm^{-1} [A_{1g} (Γ)], five additional Raman peaks were detected at 226 cm^{-1}, 272 cm^{-1}, 303 cm^{-1}, 360 cm^{-1}, and 432.5 cm^{-1}. Among these, the peak at 303 cm^{-1} is attributed to the transverse acoustic (TA) phonon mode originating from the underlying silicon substrate [16, 17]. The peak observed at 226 cm^{-1} [LA(M)] has been previously attributed to the partial oxidation of MoS_2 upon exposure to ambient conditions, leading to the formation of molybdenum oxides [18, 19]. Additionally, the peak 272 cm^{-1} has been linked to the vibrational energy states of MoO_3, suggesting oxidation (e.g., MoS_2 + 3/2 $O_2 \rightarrow MoO_3 + 2\ SO_2$) that can occur under higher laser power (5 mW) [19]. Further, we detected another the defect-induced peak at ~360 cm^{-1} which has been assigned to the transverse optical (TO) branch at the M point as reported by Sandro Mignuzzi et al. [18]. We have not yet identified the peak at 432.5 cm^{-1}, which remains under investigation.

In contrast, the FWHM values for MoS_2 on the SiO_2/Si substrate were slightly higher, measuring 6.1 cm^{-1} for the $E^1_{2g}(\Gamma)$ mode and 8.4 cm^{-1} for the $A_{1g}(\Gamma)$ mode. These findings indicate that the MoS_2 layers on sapphire exhibit better crystallinity compared to those on SiO_2/Si.

The PL spectra of MoS_2 grown on both substrates (Fig. 2 and 3) found exhibit three characteristic peaks - designated as A^-, A, and B - corresponding to the trion, the direct bandgap exciton, and the excitonic transition associated with valence band splitting due to spin-orbit coupling in MoS_2, respectively [25, 26]. The spin-orbit splitting is 164 meV for MoS_2 on SiO_2/Si which is higher than the value (152 meV) reported for the monolayer of MoS_2 [30]. This can be due to slow and small structural changes by aging or the strains underlying SiO_2/Si substrate.

References

30. X. Liang, C. Qin, Y. Gao, S. Han, G. Zhang, R. Chen, J. Hu, L. Xiao and S. Jia, Nanoscale **13** (19), 8966-8975 (2021). https://doi.org/10.1039/D1NR00019E